Article

Individual and Simultaneous Electrochemical Detection of Allura Red and Acid Blue 9 in Food Samples Using a Novel La$_2$YCrO$_6$ Double Perovskite Decorated on HLNTs as an Electrocatalyst

Published as part of ACS Omega virtual special issue "At the Speed of Light: Recent Advances in Optoelectronics".

Srujan Basavapura Ravikumar, Sanjay Ballur Prasanna, Santhosh Arehalli Shivamurthy,* Sandeep Shadakshari,* Bhari Mallanna Nagaraja, Jothi Ramalingam Rajabathar, Hamad A. Al-lohedan, and Selvaraj Arokiyaraj

Read Online

ACCESS | Metrics & More | Article Recommendations | SI Supporting Information

ABSTRACT: The present study involved the synthesis of La$_2$YCrO$_6$ double perovskites using a sol−gel approach. Additionally, a sonication method was implemented to prepare La$_2$YCrO$_6$ double perovskites decorated on halloysites (La$_2$YCrO$_6$/HLNTs). The La$_2$YCrO$_6$/HLNTs exhibited remarkable conductivity, electrocatalytic activity, and rapid electron transfer. It is imperative to possess these characteristics when overseeing the concurrent identification of Allura red (AR) and acid blue 9 (AB) in food samples. The development of the La$_2$YCrO$_6$/HLNTs was verified through the utilization of diverse approaches for structural and morphological characterization. The electrochemical techniques were employed to evaluate the analytical techniques of La$_2$YCrO$_6$/HLNTs. Impressively, the La$_2$YCrO$_6$/HLNTs demonstrated exceptional sensitivity, yielding the lowest detection limit for AR at 8.99 nM and AB at 5.14 nM. Additionally, the linear concentration range was 10−120 nM (AR and AB). The sensor that was developed exhibited remarkable selectivity, and the feasibility of AR and AB in the food sample was effectively monitored, resulting in satisfactory recoveries.
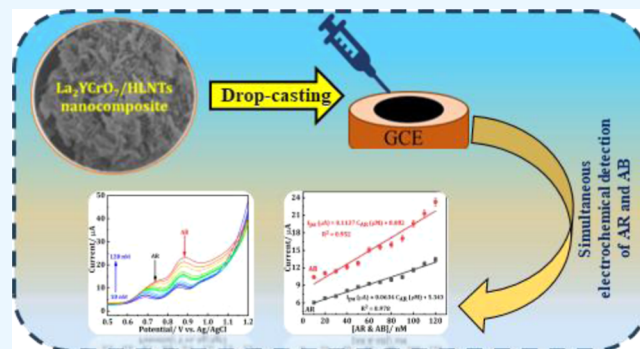
1. INTRODUCTION

Food colorants, also known as dyes, are utilized in the food industry to add color, maintain freshness, and improve the visual appeal of various food products. These additives serve both commercial and aesthetic purposes. Colorants are being used in the food sector to grab customers' attention through bright and appealing designs. Food colorants occur in a variety of characteristics, including synthetic, soluble, and so on. Producers choose the least priced and most stable options.[1] The application of these dyes continuously raises concerns about the welfare of human and environmental health. The licensing of food colorants is strictly regulated by the European Food Safety Authority (EFSA) and the US Food and Drug Administration (FDA) to guarantee the safety of food products, as these regulatory bodies acknowledge the potential long-term detrimental effects that such additives may have on consumers.[2] Specific critical values indicate amounts of additive exposure that are safe.[3] The most popular food dyes are azo-dyes [tartrazine, carmoisine, sunset yellow, Allura red (AR), acid blue 9 (AB), and so on].[4] Previous studies have

demonstrated that the molecular composition of azo dyes can lead to unwanted effects, including headaches and possible neurotoxic, genotoxic, and carcinogenic consequences.[5] AR and AB are among the most employed food dyes, and they are frequently utilized together in culinary preparations. Nevertheless, their high occurrence in environmental sources and food items poses a significant threat of exposure.[6]

In this regard, it is required to develop reliable analytical methods that allow the detection of AR and AB in different biological fluids at broad therapeutic concentrations. Several methods were employed for AR and AB analysis in different media based on different techniques such as spectrophotometric methods, HPLC, electrochemical methods, chemilumi-
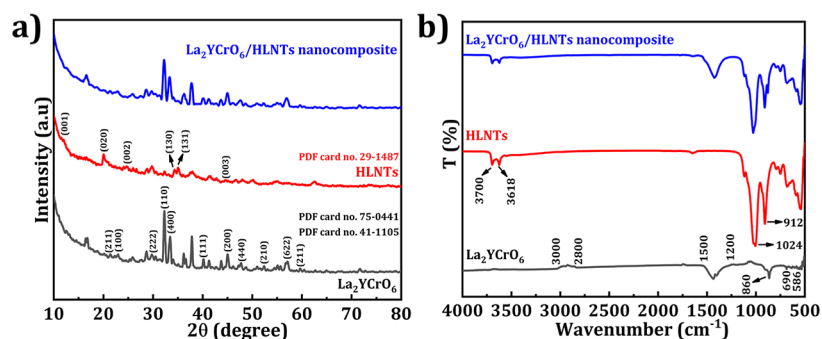
Figure 1. (a) XRD, (b) FTIR spectra of La_2YCrO_6 double perovskites, HLNTs, and La_2YCrO_6/HLNT nanocomposite.

nescence, etc.[7−9] Electrochemical sensing is a potential technology for detecting small quantities of chemicals that has a few advantages. As a result, developing novel sensor materials with electrocatalyst capabilities that can enhance existing electrodes is essential.[10] As a result, we created an accurate and low-cost monitoring method for AB and AR.

In recent years, considerable research efforts have been directed toward the study of double perovskite oxides, which possess the chemical formula $A_2B'B''O_6$.[11] The A site of the perovskite structure can accommodate either a rare-earth or an alkaline earth element, while the B site allows for the presence of two distinct transition metal (TM) elements. This unique arrangement provides a remarkable level of flexibility and freedom, surpassing that of a simple ABO_3 perovskite structure.[12−16] The electrical behavior of oxides that contain transition metals is predominantly determined by the interplay between the cations of the transition metals and the anions of oxygen.[17] Layered double perovskites, namely, $ReCuM_2O_{5+\delta}$ (Re = La, Pr, Sm, Nd, Gd, Y; M = Zr), have garnered significant scientific interest in recent times due to their efficient oxygen-ion transport and surface exchange capabilities.[18−21] Rare-earth-based double perovskites have garnered significant attention across various domains, including spintronics, catalysis, magnetic materials, photodetectors, supercapacitors, and electrode materials.[22−27] Sr_2NiMoO_6 double perovskites were synthesized by Liu et al. through the sol−gel method and subsequently employed as gas sensors.[28] Durai and Badhulika published the first solid-state synthesis of Al_2NiCoO_5 nanoflakes for atrazine electrochemical detection.[29] La_2MMnO_6 double perovskites have been synthesized by Bhardwaj et al. as an electrode material to sense nitric oxide.[30] To date, no information has been published regarding the presence of La_2YCrO_6-based double perovskites.

The distinctive structure and improved conductivity of materials possessing one-dimensional (1D) structures offer significant advantages in facilitating electrocatalytic processes for electrochemical sensors.[31] Halloysite nanotubes (HLNTs) are made up of several sheets of aluminosilicate clay.[31] HLNTs have an external siloxane (Si−O−Si) group and an internal aluminol (AleOH) group.[32] Bharathi and Wang investigated the potential of a bismuth sulfide/functionalized HLNT composite as an electrochemical device for diethofencarb analysis.[33] Radha and Wang have published work on developing hybrid 4-(methylamino)phenol (metol) electrodes made of functionalized HLNTs and lanthanum stannate for environmental sample analysis.[32] A sonochemical method was employed to synthesize a nanocomposite of La_2YCrO_6/

HLNTs, which was utilized for the concurrent detection of AR and AB in food samples.

In the present study, a highly effective electrochemical sensor can detect AR and AB individually and simultaneously. This was achieved by utilizing a modified glassy carbon electrode (GCE) with La_2YCrO_6/HLNTs. The La_2YCrO_6 double perovskites were synthesized through a sol−gel method, while the La_2YCrO_6/HLNTs were fabricated by using a sonication technique. Based on the electrochemical experiments conducted, it has been observed that the La_2YCrO_6/HLNTs/GCE exhibits enhanced conductivity, greater stability, the most minimal detection limit, and remarkable selectivity for detecting AR and AB. Additionally, the feasibility of the La_2YCrO_6/HLNTs sensor was developed to evaluate the food samples.

2. EXPERIMENTAL SECTION

Chemicals and reagents, instruments, and synthesis of the La_2YCrO_6 double perovskite details are provided in the Supporting Information (Sections S1−S3).

2.1. Preparation of the La_2YCrO_6/HLNT Nanocomposite. An aluminosilicate clay mineral generally called halloysite was used to enhance the physicochemical properties of the La_2YCrO_6 double perovskite. For the synthesis of the product with enhanced properties, 0.917 g of the product was combined with 0.915 g of halloysite in 20 mL of ethanol. The mixture was subsequently subjected to a sonication technique for 20 min to ensure thorough blending. Following this, the blend underwent thermal heating in a hot air oven set at a temperature of 57 °C. The nanocomposite formed by combining La_2YCrO_6 with HLNTs is commonly referred to as the La_2YCrO_6/HLNT nanocomposite.

2.2. Electrochemical Procedure. The electrode polishing kit PK-3 was utilized to thoroughly polish the GCE before proceeding with electrode modification. To eliminate particles and contaminants that were weakly bonded, the polished electrode underwent a series of sonication cycles with deionized water. Following this, the sample was carefully dried in a nitrogen environment to ensure thorough removal of any residual moisture and impurities. The modified electrode was formed by depositing a 6 μL solution of the synthesized nanocomposite onto the exposed surface of the bare GCE and allowing it to solidify at ambient temperature. The label on the electrode denoted its modification and identified it as La_2YCrO_6/HLNTs/GCE. The voltammetry measurements were conducted using a set of three electrodes. In this three-electrode configuration, a GCE was utilized as the working electrode, a platinum wire was utilized as the counter electrode, and a saturated calomel electrode was utilized as
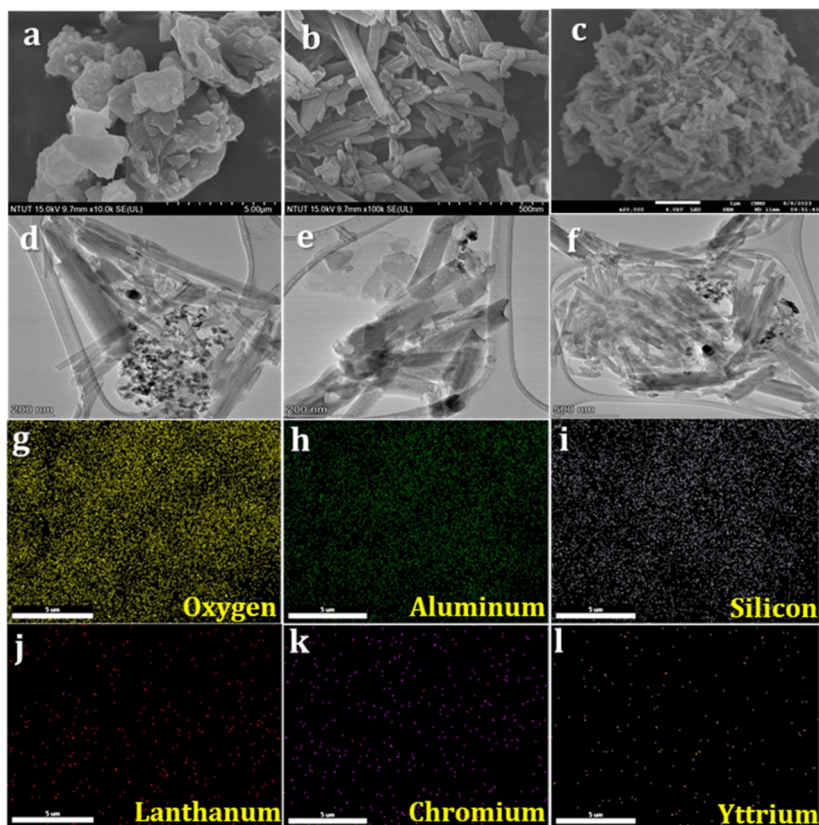
Figure 2. SEM images of the (a) La$_2$YCrO$_6$ double perovskite, (b) HLNTs, and (c) La$_2$YCrO$_6$/HLNT nanocomposite. (d−f) TEM images of the La$_2$YCrO$_6$/HLNT nanocomposite and elemental mapping of (d) O, (e) Al, (f) Si, (g) La, (h) Cr, and (i) Y of the La$_2$YCrO$_6$/HLNT nanocomposite.

the reference electrode. For the electrochemical investigations, 10 mL of 0.1 M PBS was employed. The CV analysis was conducted by scanning a voltage range from −0.8 to +1.0 V at a scan rate of 5 mV s^{-1}. To attain significant redox peaks, electrochemical impedance spectroscopy (EIS) was carried out while $[Fe(CN)_6]^{3-/4-}$ was present. The linear sweep voltammetry (LSV)was conducted using a pulse height of 200 mV and a pulse width of 0.05 s, covering a voltage range of 0 to 1.2 V.

3. RESULTS AND DISCUSSION

3.1. Characterizations. X-ray diffraction (XRD) is a formidable technique that can be employed to determine the purity of the crystal structures. It ensures the disclosure of the texture and orientation of the crystallites, thereby verifying the size and formation of the product. Figure 1a depicts the XRD examination conducted on double perovskite La$_2$YCrO$_6$, HLNTs, and the nanocomposite of La$_2$YCrO$_6$/HLNTs. LaCrO$_3$ with a perovskite crystal structure belongs to the cubic LaCrO$_3$ (PDF card no. 75-0441), and the characteristic diffraction peaks at 22.95, 32.7, 40.05, 45,12, 52.42, and 59.64° are in good agreement with the (100), (110), (111), (200), (210), and (211) planes, respectively.[34] The peaks at 23.3, 29.7, 33.4, 47.67, and 57.1° correspond to (211), (222), (400), (440), and (622) planes of Y$_2$O$_3$, respectively.[35] The (001), (020), (002), (130), (131), and (003) planes of HLNTs are attributed to the 2θ values of the diffraction peaks at 11.9, 20.1, 24.7, 34.3, 35.13, and 45.6° (JCPDS card 29-1487), respectively.[36] Additionally, the XRD patterns of the La$_2$YCrO$_6$/HLNT nanocomposite exhibit the presence of

regenerated La$_2$YCrO$_6$ and HLNTs, providing evidence for the successful synthesis of the La$_2$YCrO$_6$/HLNT nanocomposite.

Figure 1b illustrates the FTIR analysis, which elucidates the spectrum of peaks corresponding to our samples, namely, La$_2$YCrO$_6$, HLNTs, and La$_2$YCrO$_6$/HLNT nanocomposite. The absorption bands observed in the FTIR spectra correspond to the stretching vibrations of La−O and Cr−O, with strong signals at 586 and 690 cm^{-1}, respectively. The range between 1200 and 1500 cm^{-1} is commonly associated with distortion of water molecules. The H−O−H stretch observed at 2800−3000 cm^{-1} corresponds to the peak perceived in the spectrum, indicating the presence of an adsorbed water molecule.[37] The peaks observed at approximately 860 cm^{-1} were assigned to the vibrations originating from Y−O bonds.[38] The HLNTs are made up of Si−O−Si groups with Al−OH groups presented. Peaks at 3770 and 3618 cm^{-1} in the pristine HLNTs spectra correlate to the Al−OH group's stretching vibration on HLNTs. The 1024 and 912 cm^{-1} peaks correspond to Al−OH Si−O stretching and bending vibrations, respectively.[39] The successful formation of the La$_2$YCrO$_6$/HLNT nanocomposite is confirmed by the regenerated La$_2$YCrO$_6$ and HLNT bands observed in the FTIR spectra.

The morphological characteristics of the La$_2$YCrO$_6$ double perovskite, HLNTs, and La$_2$YCrO$_6$/HLNT nanocomposites were thoroughly investigated using SEM and TEM techniques. The SEM images of La$_2$YCrO$_6$ double perovskite, HLNTs, and La$_2$YCrO$_6$/HLNT nanocomposite are depicted in Figure 2a−c. In Figure 2a, the even arrangement of the La$_2$YCrO$_6$ double perovskite is depicted, with each particle displaying a distinct
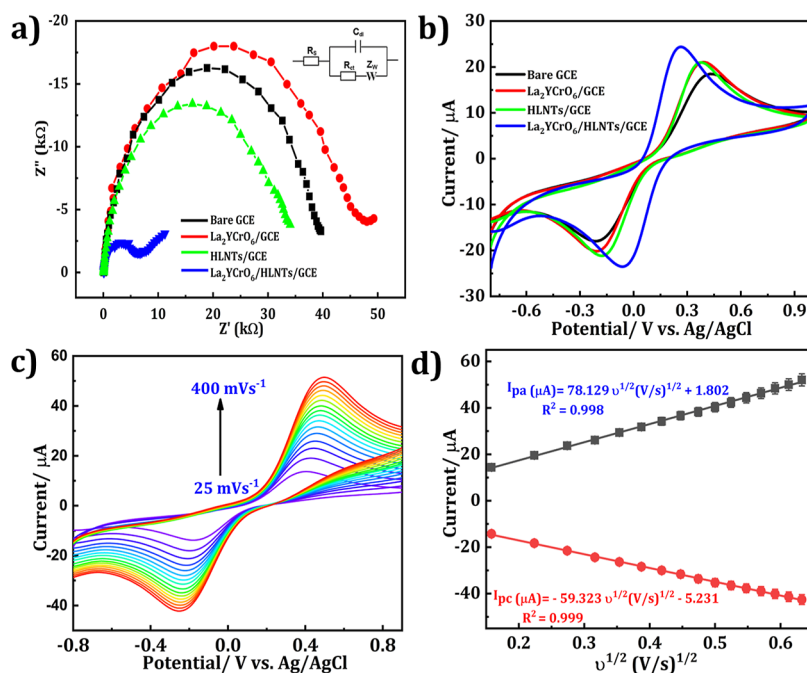
Figure 3. (a) EIS, (b) CV spectra of bare GCE, La$_2$YCrO$_6$/GCE, HLNTs/GCE, and La$_2$YCrO$_6$/HLNTs/GCE and (a-inset) Randle's equivalent circuit image, (c) different v (25−400 mV s^{-1}) at La$_2$YCrO$_6$/HLNTs/GCE and (d) $v^{1/2}$ vs I_{pc} and I_{pa}.

flake-like morphology. The tubelike structure of HLNTs is depicted in Figure 2b. Additionally, the formation of the La$_2$YCrO$_6$ /HLNT nanocomposite is confirmed by the random decoration of the La$_2$YCrO$_6$ double perovskites on the HLNTs, as depicted in Figure 2c. Figure 2d−f shows various magnification TEM images of the La$_2$YCrO$_6$/HLNT nanocomposite. The elemental mapping (O, Al, Si, La, Cr, and Y) images of the La$_2$YCrO$_6$/HLNT nanocomposite are shown in Figure 2g−l. The EDS spectra of the La$_2$YCrO$_6$/HLNT nanocomposite (Figure S1) indicate the presence of various elements and their respective mass fractions (Figure S1, inset). The oxygen, aluminum, silicon, lanthanum, chromium, and yttrium elements account for 58.21, 16.33, 19.32, 2.09, 1.35, and 2.69% of the composition, respectively. Consequently, the morphological observations authenticate the progress made in the development of a nanocomposite consisting of La$_2$YCrO$_6$/HLNTs.

3.2. Electrochemical Performance. The CV and EIS techniques were employed to investigate the electron transport parameters of the electrode contact, with a scan rate of 50 mV s^{-1} and 5.0 mM of [Fe(CN)$_6$]$^{3-/4-}$. The EIS spectra of four different materials, namely, bare GCE, La$_2$YCrO$_6$ double perovskite, HLNTs, and La$_2$YCrO$_6$/HLNT nanocomposite, are presented in Figure 3a, and Randle's circuit picture is given in Figure 3a (inset). The Nyquist plot displayed R_{ct} values of 38.85 kΩ for the bare GCE, 47.77 kΩ for La$_2$YCrO$_6$/GCE, and 33.73 kΩ for HLNTs/GCE. The La$_2$YCrO$_6$/GCE exhibited a higher R_{ct} compared to the bare GCE, indicating the presence of repulsion between the metal oxides and the redox probe [Fe(CN)$_6$]$^{3-/4-}$.[10] A substantial decrease in R_{ct} (6.54 Ωk) was observed for La$_2$YCrO$_6$/HLNTs/GCE. La$_2$YCrO$_6$/HLNTs/GCE exhibits remarkable charge-transfer properties and conductivity, making it highly advantageous for electrochemical sensing applications.

The CV curves of the bare GCE, La$_2$YCrO$_6$/GCE, HLNTs/GCE, and La$_2$YCrO$_6$/HLNTs/GCE are shown in Figure 3b.

The peak currents and electron-transfer efficiency were greater in La$_2$YCrO$_6$/HLNTs/GCE than in the bare GCE, La$_2$YCrO$_6$/GCE, and HLNTs/GCE, suggesting faster electron transfer. The behavior of La$_2$YCrO$_6$/HLNTs/GCE was analyzed under varying scan rates (v) to determine the electrode kinetics. Figure 3c illustrates the electrochemical characteristics of the La$_2$YCrO$_6$/HLNTs/GCE over a range of 25 to 400 mV/s. The values of I_{pa} and I_{pc} showed a noticeable rise as v increased. Figure 3d depicts a plot of $v^{1/2}$ (V/s)$^{1/2}$ vs I_{pa} and I_{pc}, with the related equations (eqs 1 and 2) as follows

$$I_{pa}(\mu A) = 78.129v^{1/2} \, (V/s)^{1/2} + 1.802 \qquad (R^2 = 0.998)$$
$$(1)$$

$$I_{pc}(\mu A) = -59.323v^{1/2} \, (V/s)^{1/2} - 5.231$$
$$(R^2 = 0.999)$$
$$(2)$$

The surface areas of bare GCE and La$_2$YCrO$_6$/HLNTs/GCE were also calculated using the Randles−Sevcik equation (eq 3)[40]

$$I_p = (2.69 \times 10^5)n^{3/2}A_0D_R^{1/2}v^{1/2}C_0$$
$$(3)$$

where I_{pa} = oxidation peak current, A = surface area, D = diffusion coefficient (6 × 10^{-6} cm s^{-1}), n = number of electrons, and C = electrolyte concentration (0.005 mol L^{-1}). The surface areas of bare GCE, La$_2$YCrO$_6$/GCE, HLNTs/GCE, and La$_2$YCrO$_6$/HLNTs/GCE were calculated using eq 3 to be 0.225, 0.256, 0.254, and 0.296 cm^2, respectively. In this regard, La$_2$YCrO$_6$/HLNTs/GCE exhibits a significant reactive site due to its extensive surface area.

To analyze the kinetics of the oxidation process and electrode reaction, the influence of the scan rate on the sensing of 50 μM AR and AB in 0.1 M PB (pH 7) was investigated using La$_2$YCrO$_6$/HLNTs/GCE. Figure 4a displays the CV findings for AR and AB, obtained by varying the v from 20 to 375 mV/s. Notably, the redox peak current demonstrates
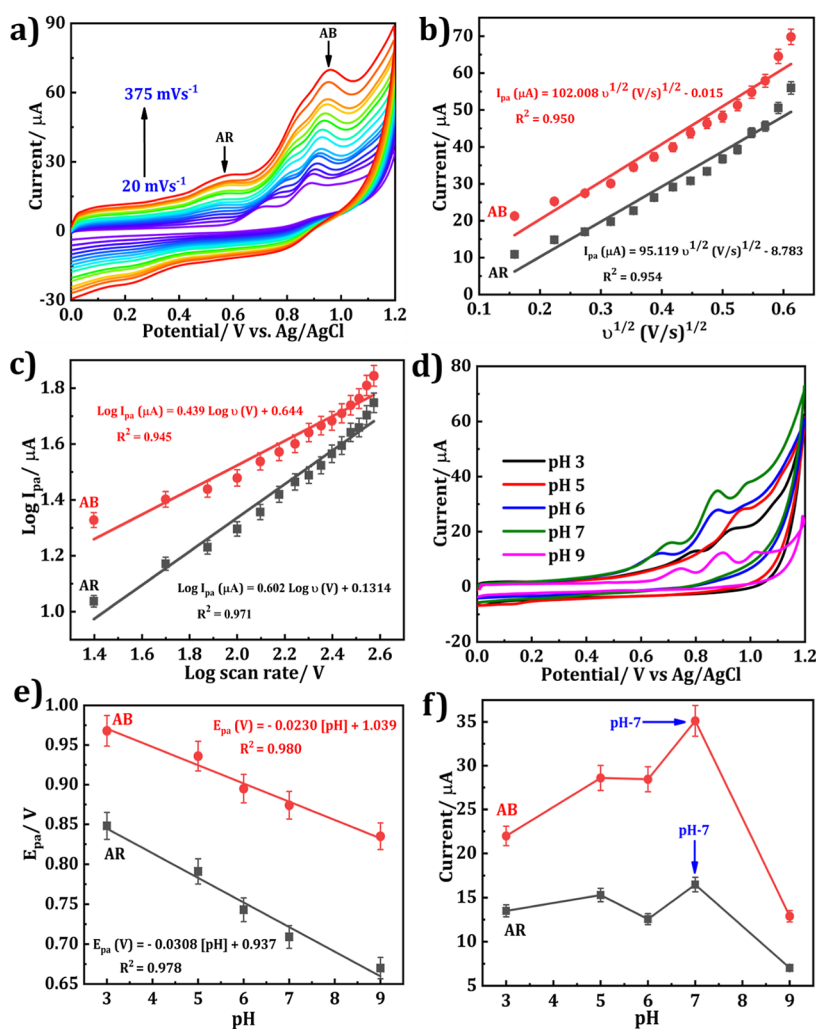
Figure 4. (a) CV graphs for v (20−375 mV s^{-1}) in 50 μM AR and (b) $v^{1/2}$ (V/s)$^{1/2}$ vs I_{pc} (AR and AB) and (c) log v vs log I_{pc} (AR and AB). (d) CV response of La$_2$YCrO$_6$/HLNTs/GCE with different pH values, (e) pH vs E_{pa}, and (f) pH vs I_{pc} of La$_2$YCrO$_6$/HLNTs/GCE.

a consistent linear rise with the increase in v. Using regression (eqs 4 and 5), a significant linear relationship between oxidation peak current and square root of scan rates was established, as illustrated in Figure 4b.

$$I_{pa}(\mu A) = 95.119 v^{1/2} (V/s)^{1/2} - 8.783$$
$$(R^2 = 0.954: AR) \tag{4}$$

$$I_{pa}(\mu A) = 102.008 v^{1/2} (V/s)^{1/2} - 0.015$$
$$(R^2 = 0.950: AB) \tag{5}$$

The electro-oxidation of AR and AB occurred in diffusion-controlled processes within the La$_2$YCrO$_6$/HLNTs/GCE system. The log vs log I_{pa} (Figure 4c) was obtained, and eqs 6 and 7 were derived accordingly

$$Log I_{pa}(\mu A) = 0.602 \log v(V) + 0.1314$$
$$(R^2 = 0.971: AR) \tag{6}$$

$$Log I_{pa}(\mu A) = 0.439 \log v(V) + 0.644$$
$$(R^2 = 0.945: AB) \tag{7}$$

The slopes of AR and AB were determined to be around 0.602 and 0.439, respectively, based on eqs 6 and 7. These values are near the expected theoretical value of 0.5.[41] The findings provide support for the notion that the diffusion-controlled process underlies the electro-oxidation of AR and AB.

The pH level of the PBS solution has a substantial impact on the current response of AR and AB toward La$_2$YCrO$_6$/HLNTs/GCE. Consequently, the study aimed to analyze the effects of different pH values on CV, employing 50 μM AR and AB. Figure 4d illustrates that the I_{pa} values of AR and AB exhibit a consistent increase as the pH level rises from 3 to 7. This observation implies that sensitivity can potentially be enhanced by this pH elevation. At pH 7, the I_{pa} levels of AR and AB are the highest, while the current responses decrease as the pH rises to 9. Consequently, pH 7 was chosen as the most suitable electrolyte to facilitate further investigations. Furthermore, as the pH changed from 3 to 9, the E_{pa} of analytes (AR and AB) shifted slightly to the negative side, suggesting that H$^+$ are engaged in the electrochemical response of AR and AB at La$_2$YCrO$_6$/HLNTs/GCE sensor.[42] Figure 4e shows the linear plots of pH vs E_{pa} for AR and AB, as well as the corresponding (eqs 8 and 9).
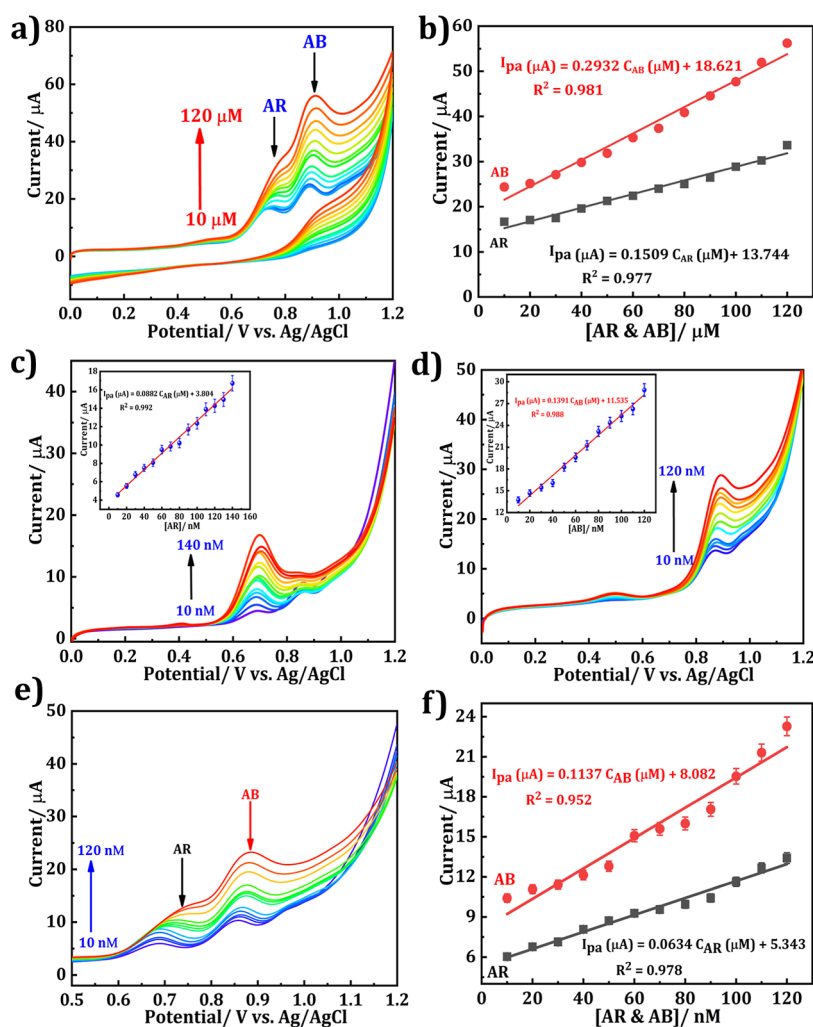
Figure 5. (a) CV responses with simultaneously increasing AR and AB concentrations (10−120 μM) on the La$_2$YCrO$_6$/HLNTs/GCE and (b) [AR and AB]/μM vs I_{pa}. (c) LSVs of individual detection of AR and (d) AB at the different concentrations on La$_2$YCrO$_6$/HLNTs/GCE, and (c: inset) [AR]/nM vs I_{pa} with various additions from 10 to 140 nM and (d: inset) [AB]/nM vs I_{pa} with various additions from 10 to 120 nM. (e) LSV graph of simultaneous detection of 10 to 120 nM AR and AB in pH 7 (0.1 M PBS). (f) [AR/AB]/nM vs I_{pa}.

$$E_{pa}(V) = -0.0308[pH] + 0.937 \qquad (R^2 = 0.978: AR) \tag{8}$$

$$E_{pa}(V) = -0.0230[pH] + 1.039 \qquad (R^2 = 0.980: AB) \tag{9}$$

The graphs of pH vs I_{pa} for AR and AB are shown in Figure 4f. Consequently, pH 7 was selected as the optimal supportive electrolyte for further investigations into the individual and simulated detection of AR and AB.

The electroanalytical properties of La$_2$YCrO$_6$/HLNTs/GCE were investigated at increasing concentrations (10−120 μM) of AR and AB. The I_{pa} values steadily increased with increasing AR and AB concentrations (Figure 5a). The calibration graph (Figure 5b) is drawn between the AR and AB concentrations and the corresponding I_{pa}. Resulting, the equations (eqs 10 and 11) are as follows

$$I_{pa}(\mu A) = 0.1509\, C_{AR}(\mu M) + 13.744$$

$$(R^2 = 0.977: AR) \tag{10}$$

$$I_{pa}(\mu A) = 0.2932\, C_{AB}(\mu M) + 18.621$$

$$(R^2 = 0.981: AB) \tag{11}$$

The La$_2$YCrO$_6$/HLNTs/GCE showed higher electrochemical activity toward the simultaneous detection of AR and AB due to their improved conductivity and electrocatalytic activity.

3.3. Individual and Simultaneous Detection. The LSV approach is exceptionally sensitive and well-selected compared to other electroanalytical processes. By incrementing one analyte at a time, AR and AB were examined independently, and subsequently, both were simultaneously detected in 0.1 M PBS (pH 7) using the LSV technique. In Figure 5c,d, the LSV curves exhibit the detection of individual analytes of AR and AB concentration range of 10 to 140 and 10 to 120 nM, respectively. The concentration of AR and AB in Figure 5c,d (inset) shows a linear increase in response to the increasing I_{pa}. This relationship is described by linear equations (eqs 12 and 13)

$$I_{pa}(\mu A) = 0.0882\, C_{AR}(\mu M) + 3.804$$

$$(R^2 = 0.992: AR) \tag{12}$$

Table 1. Comparison of the Electrochemical Oxidation of AR Using La$_2$YCrO$_6$/HLNTs/GCE with Other Materials

electrode material	method	pH	linear range (μM)	LOD (NM)	references
TiO$_2$/ErGO	DPV	7	0.3−800	50	43
F-nanodiamond@SiO$_2$@TiO$_2$	DPV	3	0.01−8.65	1.22	44
SHU/PCFE	LSV	4	0.01−2	0.36	45
LaOX-TiOX/CPE	SWV	2.5		90	46
Mn$_3$O$_4$@C/SPM	DPV		0.1−1748.4	0.3	47
La$_2$YCrO$_6$/HLNTs/GCE	**LSV**	**7**	**10−120**	**8.99**	**present work**

Table 2. Comparison of the Electrochemical Oxidation of AB and Food Additives Using La$_2$YCrO$_6$/HLNTs/GCE with Other Materials

electrode material	method	pH	linear range (μM)	LOD (nM)	references
IL/Cu-BTC MOF//CPE	DPV	7	0.08−900	70	48
IL/AuTiO$_2$/GO/CPE	DPV	2	1−1000	330	49
MIPMet/CFP	DPV	4	0.0006−0.16	0.027	50
Co$_3$O$_4$ NRs/FCB	DPV	7	0.12−62.2	1	51
PASPMGN/CPE	DPV	7	1.0−15.0	4850	52
La$_2$YCrO$_6$/HLNTs/GCE	**LSV**	**7**	**10−120**	**5.14**	**present work**
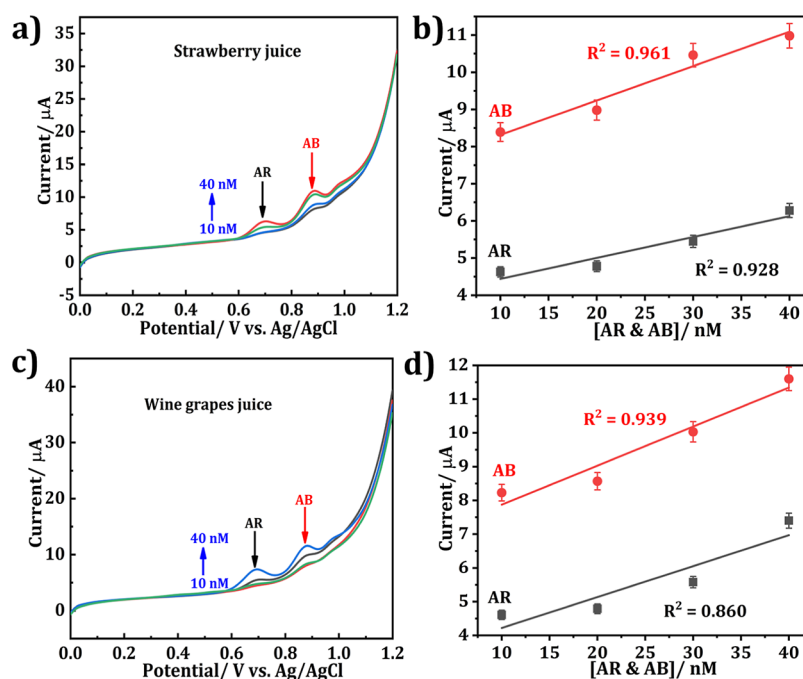
Figure 6. LSV responses of the AR and AB in (a) strawberry juice, (c) wine juice, and (b,d) corresponding correlation graphs of fruit samples.

$$I_{pa}(\mu A) = 0.1319\, C_{AB}\,(\mu M) + 11.535$$

$$(R^2 = 0.988:\ AB) \tag{13}$$

Furthermore, the LSV profiles of La$_2$YCrO$_6$/HLNTs/GCE for the simultaneous determination of AR and AB, ranging from 10 to 120 nM, are depicted in Figure 5e. The catalytic activity of the La$_2$YCrO$_6$/HLNTs/GCE sensor was demonstrated by the considerable increase in the I_{pa} of AR and AB with the simultaneous increase in their concentrations. These results provide strong evidence of the sensor's high sensitivity in detecting AR and AB. Linear plots (Figure 5f) were employed to visualize the concentrations of [AR/AB]/nM and I_{pa} and their linear equations (eqs 14 and 15)

$$I_{pa}(\mu A) = 0.0634\, C_{AB}\,(\mu M) + 5.343$$

$$(R^2 = 0.978:\ AR) \tag{14}$$

$$I_{pa}(\mu A) = 0.1137\, C_{AB}(\mu M) + 8.082$$

$$(R^2 = 0.952:\ AB) \tag{15}$$

The limit of detection (LOD) for AR and AB when measured simultaneously (10−120 nM) was found to be 8.99 and 5.14 nM, respectively. On the other hand, the estimated LOD for AR alone (10−140 nM) was determined to be 5.78, while for AB it was 4.3 nM. The LOD values closely mirrored those obtained methods. The estimated sensitivity of the individual was found to be 0.905 μA μM^{-1} cm^{-2} for AR (10−140 nM) and 1.62 μA μM^{-1} cm^{-2} for AB (10−120 nM), indicating a significant difference between the individual and simultaneous methods. As a result, the developed La$_2$YCrO$_6$/HLNTs/GCE platform provides a better determination platform for either simultaneous or individual detection of selective dyes (AR and AB). This study revealed that the

modified La$_2$YCrO$_6$/HLNTs/GCE exhibited enhanced sensitivity and low LOD for the detection of AR and AB. The La$_2$YCrO$_6$/HLNTs/GCE results showed exceptional performance in comparison to other available detection materials when compared with earlier AR (Table 1) and AB (Table 2) results.

3.4. Selectivity, Repeatability, and Storage Stability.

For the simultaneous detection of biological, dye, and metal compounds, a high degree of selectivity is required. The sensitivity of AR and AB detection was investigated by analyzing their responses in the presence of various competing species. LSV curves were obtained by adding 200 μM of citric acid (CA), glucose (Glu), sunset yellow (SY), tartrazine (TTZ), calcium chloride (Ca^{2+}), zinc chloride (Zn^{2+}), copper chloride (Cu^{2+}), and sodium chloride (Cl$^-$) to a solution (50 μM of AR and AB) (Figure S2a). The suggested analytes in all I_{pa} responses exhibit no noticeable differences, with their signals fluctuating by less than 6%. The results indicate that La$_2$YCrO$_6$/HLNTs/GCE is an appropriate sensor for accurately detecting AR and AB in the presence of biological, dye, and metal interferences.

Furthermore, an examination was conducted to assess the reproducibility by employing a La$_2$YCrO$_6$/HLNTs/GCE (Figure S2b). The obtained RSD values for AR (2.24%) and AB (2.9%) indicate that La$_2$YCrO$_6$/HLNTs/GCE demonstrated excellent repeatability. Figure S2c illustrates the LSV curves, which were used to evaluate the stability of the system from 1 to 15 days. It demonstrates that after 15 days of storage, 67.05% (AR) and 73.69% (AB) of the initial value is retained. Figure S2d shows a bar depiction of the number of days vs the current date. The simultaneous detection of AR and AB was achieved with exceptional stability by the La$_2$YCrO$_6$/HLNTs/GCE system, as indicated by these findings.

3.5. Real Sample Analysis of AR and AB.

Strawberry and wine grape juice were purchased from street vendors in Bangalore, Karnataka, India. Following a centrifugation period of 10 min at 6000 rpm, the mixture was subjected to separation. The resulting supernatant, collected post-centrifugation, was then stored at a temperature of 4 °C to facilitate future analysis. By utilizing the La$_2$YCrO$_6$/HLNTs/GCE, the practical feasibility of the juice samples was evaluated. To assess the juice samples, a dilution was carried out using PBS (pH 7), and then, AR and AB were added at the specified concentrations using the standard addition method. Figure 6a illustrates the responses of the AR and AB-spiked strawberry juice samples, while Figure 6b showcases the corresponding linear plot. The linear regression equations are represented by eqs 16 and 17, as mentioned below

$$I_{pa}\ (\mu A) = 0.0562\ C\ (\mu A) + 3.88 \qquad (R^2 = 0.961:\ AR) \tag{16}$$

$$I_{pa}\ (\mu A) = 0.0925\ C\ (\mu A) + 7.39 \qquad (R^2 = 0.928:\ AB) \tag{17}$$

Figure 6c illustrates the responses of the wine grape samples spiked with AR and AB, while Figure 6d shows the corresponding linear plot. The equations are represented by eqs 18 and 19, as shown below

$$I_{pa}\ (\mu A) = 0.0562\ C\ (\mu A) + 3.88 \quad (R^2 = 0.961:\ AR) \tag{18}$$

$$I_{pa}\ (\mu A) = 0.0562\ C(\mu A) + 3.88 \quad (R^2 = 0.961:\ AB) \tag{19}$$

Table S1 summarizes the recovery findings. The results indicated that La$_2$YCrO$_6$/HLNTs/GCE exhibited satisfactory recoveries when detecting both AR and AB simultaneously in fruit samples.

4. CONCLUSIONS

In this work, we introduced a highly effective electrochemical sensor that utilizes a La$_2$YCrO$_6$/HLNT-modified GCE to detect both AR and AB individually and simultaneously. The La$_2$YCrO$_6$/HLNTs/GCE demonstrated the electro-oxidation of AR and AB in two fruit samples. Moreover, the LSV response of the sensor exhibited robust linearity in the 10 to 120 nM (AR) range, with a LOD of 1.26 nM. Additionally, the sensor displayed strong linearity in the 10 to 120 nM (AB) range, with a LOD of 1.98 nM (AB). The proposed sensor, La$_2$YCrO$_6$/HLNTs/GCE, exhibits remarkable sensitivity with an AR value of 0.905 and an AB value of 1.62 μA μM^{-1} cm^{-2}. Moreover, La$_2$YCrO$_6$/HLNTs/GCE exhibited remarkable stability, selectivity, and reproducibility. By employing LSV, La$_2$YCrO$_6$/HLNTs/GCE was utilized to measure AR and AB in fruit samples, such as strawberry juice and wine grape juice, to evaluate its applicability. The results indicated excellent recoveries and the potential of this novel sensor for the determination of AR and AB in food samples.

■ ASSOCIATED CONTENT

Ⓢ Supporting Information

The Supporting Information is available free of charge at https://pubs.org/doi/10.1021/acsomega.3c07330.

EDS analysis of La$_2$YCrO$_6$/HLNT nanocomposite, LSV performance of various interfering substances, repeatability, storage stability, and real-time application in fruit samples (PDF)

■ AUTHOR INFORMATION

Corresponding Authors

Santhosh Arehalli Shivamurthy − *Department of Chemistry (U.G.), N.M.K.R.V. College for Women, Karnataka 560011, India;* ⓞ orcid.org/0000-0002-6606-3026; Phone: +91 8861027395; Email: santhu41100@gmail.com

Sandeep Shadakshari − *Department of Chemistry, SJCE, JSS Science and Technology University, Karnataka 570006, India;* ⓞ orcid.org/0000-0003-4342-4623; Phone: +91 9591572962; Email: sandeep12chem@gmail.com

Authors

Srujan Basavapura Ravikumar − *Department of Chemistry, SJCE, JSS Science and Technology University, Karnataka 570006, India*

Sanjay Ballur Prasanna − *Department of Chemical Engineering and Biotechnology, National Taipei University of Technology (Taipei Tech), Taipei 10608, Taiwan*

Bhari Mallanna Nagaraja − *Centre for Nano and Material Science (CNMS), Jain University, Bangalore 562112, India;* ⓞ orcid.org/0000-0002-9141-0771

Jothi Ramalingam Rajabathar − *Department of Chemistry, College of Science, King Saud University, Riyadh 11451, Saudi Arabia*

Hamad A. Al-lohedan − *Department of Chemistry, College of Science, King Saud University, Riyadh 11451, Saudi Arabia*

Selvaraj Arokiyaraj − *Department of Food Science and Biotechnology, Sejong University, Seoul 05006, South Korea*

Author Contributions

S.B.R.—writing-original draft, writing-review and editing, methodology, formal analysis, data curation, and visualization. S.B.P.—writing-review and editing. B.M.N.—characterizations and methodology. J.R.R.—funding acquisition and methodology. H.S.A.-l. and S.A.—writing-review and editing, and methodology. S.A.S. and S.S.—conceptualization, methodology, supervision, project administration, funding acquisition, and writing—review and editing.

Notes

The authors declare no competing financial interest.

■ REFERENCES

(1) Yamjala, K.; Nainar, M. S.; Ramisetti, N. R. Methods for the Analysis of Azo Dyes Employed in Food Industry - A Review. *Food Chem.* 2016, 192, 813−824.

(2) Martins, N.; Roriz, C. L.; Morales, P.; Barros, L.; Ferreira, I. C. F. R. Food Colorants: Challenges, Opportunities and Current Desires of Agro-Industries to Ensure Consumer Expectations and Regulatory Practices. *Trends Food Sci. Technol.* 2016, 52, 1−15.

(3) Amchova, P.; Kotolova, H.; Ruda-Kucerova, J. Health Safety Issues of Synthetic Food Colorants. *Regul. Toxicol. Pharmacol.* 2015, 73 (3), 914−922.

(4) Amin, K. A.; Abdel Hameid, H.; Abd Elsttar, A. H. Effect of Food Azo Dyes Tartrazine and Carmoisine on Biochemical Parameters Related to Renal, Hepatic Function and Oxidative Stress Biomarkers in Young Male Rats. *Food Chem. Toxicol.* 2010, 48 (10), 2994−2999.

(5) Haridevamuthu, B.; Murugan, R.; Seenivasan, B.; Meenatchi, R.; Pachaiappan, R.; Almutairi, B. O.; Arokiyaraj, S.; M, K. K.; Arockiaraj, J. Synthetic Azo-Dye, Tartrazine Induces Neurodevelopmental Toxicity via Mitochondria-Mediated Apoptosis in Zebrafish Embryos. *J. Hazard. Mater.* 2024, 461, 132524.

(6) Darabi, R.; Shabani-Nooshabadi, M. NiFe2O4-RGO/Ionic Liquid Modified Carbon Paste Electrode: An Amplified Electrochemical Sensitive Sensor for Determination of Sunset Yellow in the Presence of Tartrazine and Allura Red. *Food Chem.* 2021, 339, 127841.

(7) Feyzi, F.; Soleymani, J.; Dastmalchi, S.; Ranjbar, F.; Jouyban, A. Dispersive Solid Phase Extraction of Risperidone from Plasma Samples Using Graphene Oxide Aerogels and Determination with Liquid Chromatography. *J. Sep. Sci.* 2023, 46, No. e2201028.

(8) Aravagiri, M.; Marder, S. R. Simultaneous Determination of Risperidone and 9-Hydroxyrisperidone in Plasma by Liquid Chromatography/Electrospray Tandem Mass Spectrometry. *J. Mass Spectrom.* 2000, 35 (6), 718−724.

(9) Aravagiri, M.; Marder, S. R.; van Putten, T.; Midha, K. K. Determination of Risperidone in Plasma by High-performance Liquid Chromatography with Electrochemical Detection: Application to Therapeutic Drug Monitoring in Schizophrenic Patients. *J. Pharm. Sci.* 1993, 82 (5), 447−449.

(10) Ballur Prasanna, S.; Sakthivel, R.; Lin, L. Y.; Duann, Y. F.; He, J. H.; Liu, T. Y.; Chung, R. J. MOF Derived 2D-Flake-like Structured Mn3Co3O4 Integrated Acid Functionalized MWCNT for Electrochemical Detection of Antibiotic Furazolidone in Biological Fluids. *Appl. Surf. Sci.* 2023, 611, 155784.

(11) Lavat, A. E.; Baran, E. J. IR-Spectroscopic Characterization of A2BB′O6 Perovskites. *Vib. Spectrosc.* 2003, 32 (2), 167−174.

(12) Berri, S. First Principle Analysis of Structural, Electronic, Optical, and Thermoelectric Characteristics of Ba3CaTa2O9 Complex Perovskite. *Emergent Mater.* 2022, 5 (6), 1849−1857.

(13) Nemla, F.; Cherrad, D. First Principles Study of Structural, Elastic, Electronic, and Optical Properties of the Cubic Perovskites AVO3 (A = Ca and La). *Emergent Mater.* 2022, 5 (1), 175−186.

(14) Winterhoff, G.; Neitzel-Grieshammer, S. A Review of Proton Migration and Interaction Energies in Doped Barium Zirconate. *Solid State Ionics* 2023, 397, 116231.

(15) Ahamed, T.; Rahaman, I.; Karmakar, S.; Halim, M. A.; Sarkar, P. K. Thickness Optimization and the Effect of Different Hole Transport Materials on Methylammonium Tin Iodide (CH3NH3SnI3)-Based Perovskite Solar Cell. *Springer* 2022, 6 (1), 175−183.

(16) Liang, L.; Cai, Y.; Gao, P. A Facile Gas-Driven Ink Spray (GDIS) Deposition Strategy toward Hole-Conductor-Free Carbon-Based Perovskite Solar Cells. *Emergent Mater.* 2022, 5 (4), 967−975.

(17) Saha-Dasgupta, T. Magnetism in Double Perovskites. *J. Supercond. Nov. Magnetism* 2013, 26 (5), 1991−1995.

(18) Chen, Y.; deGlee, B.; Tang, Y.; Wang, Z.; Zhao, B.; Wei, Y.; Zhang, L.; Yoo, S.; Pei, K.; Kim, J. H.; Ding, Y.; Hu, P.; Tao, F. F.; Liu, M. A robust fuel cell operated on nearly dry methane at 500 °C enabled by synergistic thermal catalysis and electrocatalysis. *Nat. Energy* 2018, 3 (12), 1042−1050.

(19) Anjum, U.; Khan, T. S.; Agarwal, M.; Haider, M. A. Identifying the Origin of the Limiting Process in a Double Perovskite PrBa0.5Sr0.5Co1.5Fe0.5O5+δ Thin-Film Electrode for Solid Oxide Fuel Cells. *ACS Appl. Mater. Interfaces* 2019, 11 (28), 25243−25253.

(20) Wang, L.; Xie, P.; Bian, L.; Liu, X.; Chou, K. Performance of Ca-Doped GdBa1-XCaxFe2O5+δ(X = 0, 0.1) as Cathode Materials for IT-SOFC Application. *Catal. Today* 2018, 318, 132−136.

(21) Hashim, S. S.; Liang, F.; Zhou, W.; Sunarso, J. Cobalt-Free Perovskite Cathodes for Solid Oxide Fuel Cells. *Chemelectrochem* 2019, 6 (14), 3549−3569.

(22) Raril, C.; Manjunatha, J. G. Sensitive Electrochemical Analysis of Resorcinol Using Polymer Modified Carbon Paste Electrode: A Cyclic Voltammetric Study. *Anal. Bioanal. Electrochem.* 2018, 10 (4), 488−498.

(23) Hashisaka, M.; Kan, D.; Masuno, A.; Takano, M.; Shimakawa, Y.; Terashima, T.; Mibu, K. Epitaxial Growth of Ferromagnetic La2NiMnO6 with Ordered Double-Perovskite Structure. *Appl. Phys. Lett.* 2006, 89 (3), 032504.

(24) Rajendran, D. N.; Ravindran Nair, K.; Prabhakar Rao, P.; Sibi, K. S.; Koshy, P.; Vaidyan, V. K. New Perovskite Type Oxides: NaATiMO6 (A = Ca or Sr; M = Nb or Ta) and Their Electrical Properties. *Mater. Lett.* 2008, 62 (4−5), 623−628.

(25) Hamakawa, S.; Li, L.; Li, A.; Iglesia, E. Synthesis and hydrogen permeation properties of membranes based on dense SrCe0.95Yb0.05O3− thin films. *Solid State Ionics* 2002, 148 (1−2), 71−81.

(26) Yoshimatsu, K.; Nogami, K.; Watarai, K.; Horiba, K.; Kumigashira, H.; Sakata, O.; Oshima, T.; Ohtomo, A. Synthesis and Magnetic Properties of Double-Perovskite Oxide La 2 MnFeO 6 Thin Films. *Phys. Rev. B* 2015, 91, 054421.

(27) Meng, Z.; Xu, J.; Yu, P.; Hu, X.; Wu, Y.; Zhang, Q.; Li, Y.; Qiao, L.; Zeng, Y.; Tian, H. Double Perovskite La2CoMnO6 Hollow Spheres Prepared by Template Impregnation for High-Performance Supercapacitors. *Chem. Eng. J.* 2020, 400, 125966.

(28) Liu, T.; Wang, T.; Li, H.; Su, J.; Hao, X.; Liu, F.; Liu, F.; Liang, X. Ethanol Sensor Using Gadolinia-Doped Ceria Solid Electrolyte and Double Perovskite Structure Sensing Material. *Sens. Actuators, B* 2021, 349, 130771.

(29) Durai, L.; Badhulika, S. Highly Selective Trace Level Detection of Atrazine in Human Blood Samples Using Lead-Free Double Perovskite Al2NiCoO5Modified Electrode via Differential Pulse Voltammetry. *Sens. Actuators, B* 2020, 325, 128792.

(30) Bhardwaj, A.; Bae, H.; Mathur, L.; Mathur, S.; Song, S. J. Efficient Nitric Oxide Sensing on Nanostructured La2MMnO6 (M: Co, Cu, Zn) Electrodes. *Ceram. Int.* **2023**, *49* (6), 9607−9614.

(31) Kokulnathan, T.; Wang, T. J.; Ashok Kumar, E.; Ahmed, F. Construction of Nickel Cobalt-Layered Double Hydroxide/Functionalized-Halloysite Nanotubes Composite for Electrochemical Detection of Organophosphate Insecticide. *Chem. Eng. J.* **2022**, *433*, 133639.

(32) Radha, A.; Wang, S. F. Designing Hybrid Lanthanum Stannate/Functionalized Halloysite Nanotubes as Electrode Material for Electrochemical Detection of 4-(Methylamino)Phenol (Metol) in Environmental Samples. *ACS Sustain. Chem. Eng.* **2023**, *11* (13), 5072−5081.

(33) Bharathi, P.; Wang, S. F. Integration of Bismuth Sulfide/Functionalized Halloysite Nanotube Composite: An Electrochemical Tool for Diethofencarb Analysis. *Chemosphere* **2023**, *310*, 136834.

(34) Sung, M. C.; Lee, G. H.; Kim, D. W. Efficient Li2O2 Oxidation Kinetics of Perovskite-Type Lanthanum Chromium-Based Oxide by Promoter Interface Formation for Lithium-Oxygen Batteries. *Energy Storage Mater.* **2023**, *60*, 102829.

(35) Zhang, R. B.; Tu, Z. A.; Meng, S.; Feng, G.; Lu, Z. H.; Yu, Y. Z.; Reina, T. R.; Hu, F. Y.; Chen, X. H.; Ye, R. P. Engineering Morphologies of Yttrium Oxide Supported Nickel Catalysts for Hydrogen Production. *Rare Met.* **2023**, *42* (1), 176−188.

(36) Kokulnathan, T.; Wang, T. J.; Thangapandian, M.; Alaswad, S. O. Synthesis and Characterization of Hexagonal Boron Nitride/Halloysite Nanotubes Nanocomposite for Electrochemical Detection of Furazolidone. *Appl. Clay Sci.* **2020**, *187*, 105483.

(37) Shinde, V. S.; Kapadnis, K. H.; Sawant, C. P.; Koli, P. B.; Patil, R. P. Screen Print Fabricated In3+ Decorated Perovskite Lanthanum Chromium Oxide (LaCrO3) Thick Film Sensors for Selective Detection of Volatile Petrol Vapors. *J. Inorg. Organomet. Polym. Mater.* **2020**, *30* (12), 5118−5132.

(38) Zhang, L.; Li, Z.; Zhen, F.; Wang, L.; Zhang, Q.; Sun, R.; Selim, F. A.; Wong, C.; Chen, H. High Sinterability Nano-Y2O3 Powders Prepared via Decomposition of Hydroxyl-Carbonate Precursors for Transparent Ceramics. *J. Mater. Sci.* **2017**, *52* (14), 8556−8567.

(39) Khorasanizadeh, M. H.; Ghiyasiyan-Arani, M.; Monsef, R.; Salavati-Niasari, M.; Moayedi, H. Ultrasound-Accelerated Synthesis of Uniform DyVO4 Nanoparticles as High Activity Visible-Light-Driven Photocatalyst. *Ultrason. Sonochem.* **2019**, *59*, 104719.

(40) Prasanna, S. B.; Bahajjaj, A. A. A.; Lee, Y. H.; Lin, Y. C.; Dhawan, U.; Sakthivel, R.; Chung, R. J. Highly Responsive and Sensitive Non-Enzymatic Electrochemical Sensor for the Detection of β-NADH in Food, Environmental and Biological Samples Using AuNP on Polydopamine/Titanium Carbide Composite. *Food Chem.* **2023**, *426*, 136609.

(41) Sangili, A.; Sakthivel, R.; Chen, S. M. Cost-Effective Single-Step Synthesis of Flower-like Cerium-Ruthenium-Sulfide for the Determination of Antipsychotic Drug Trifluoperazine in Human Urine Samples. *Anal. Chim. Acta* **2020**, *1131*, 35−44.

(42) Guan, Q.; Guo, H.; Xue, R.; Wang, M.; Zhao, X.; Fan, T.; Yang, W.; Xu, M.; Yang, W. Electrochemical Sensor Based on Covalent Organic Frameworks-MWCNT-NH2/AuNPs for Simultaneous Detection of Dopamine and Uric Acid. *J. Electroanal. Chem.* **2021**, *880*, 114932.

(43) Li, G.; Wu, J.; Jin, H.; Xia, Y.; Liu, J.; He, Q.; Chen, D. Titania/Electro-Reduced Graphene Oxide Nanohybrid as an Efficient Electrochemical Sensor for the Determination of Allura Red. *Nanomaterials* **2020**, *10* (2), 307.

(44) Mehmandoust, M.; Pourhakkak, P.; Hasannia, F.; Özalp, Ö.; Soylak, M.; Erk, N. A Reusable and Sensitive Electrochemical Sensor for Determination of Allura Red in the Presence of Tartrazine Based on Functionalized Nanodiamond@SiO2@TiO2; an Electrochemical and Molecular Docking Investigation. *Food Chem. Toxicol.* **2022**, *164*, 113080.

(45) Bukharinova, M. A.; Khamzina, E. I.; Stozhko, N. Y.; Tarasov, A. V. Highly Sensitive Voltammetric Determination of Allura Red (E129) Food Colourant on a Planar Carbon Fiber Sensor Modified with Shungite. *Anal. Chim. Acta* **2023**, *1272*, 341481.

(46) Vargas-Varela, A.; Cardenas-Riojas, A. A.; Nagles, E.; Hurtado, J. Detection of Allura Red in Food Samples Using Carbon Paste Modified with Lanthanum and Titanium Oxides. *ChemistrySelect* **2023**, *8*, No. e202204737.

(47) Zhang, K.; Zeng, H.; Feng, J.; Liu, Z.; Chu, Z.; Jin, W. Screen-Printing of Core-Shell Mn3O4@C Nanocubes Based Sensing Microchip Performing Ultrasensitive Recognition of Allura Red. *Food Chem. Toxicol.* **2022**, *162*, 112908.

(48) Darabi, R.; Shabani-Nooshabadi, M.; Karimi-Maleh, H.; Gholami, A. The Potential of Electrochemistry for One-Pot and Sensitive Analysis of Patent Blue V, Tartrazine, Acid Violet 7 and Ponceau 4R in Foodstuffs Using IL/Cu-BTC MOF Modified Sensor. *Food Chem.* **2022**, *368*, 130811.

(49) State, R. G.; van Staden, J. K. F.; State, R. N.; Papa, F. Rapid and Sensitive Electrochemical Determination of Tartrazine in Commercial Food Samples Using IL/AuTiO2/GO Composite Modified Carbon Paste Electrode. *Food Chem.* **2022**, *385*, 132616.

(50) George, A.; Rose Cherian, A.; Jacob, B.; Varghese, A.; Maiyalagan, T. Design Optimisation and Fabrication of Amino Acid Based Molecularly Imprinted Sensor for the Selective Determination of Food Additive Tartrazine. *Food Chem.* **2023**, *404*, 134673.

(51) Balram, D.; Lian, K. Y.; Sebastian, N.; Al-Mubaddel, F. S.; Noman, M. T. A Sensitive and Economical Electrochemical Platform for Detection of Food Additive Tert-Butylhydroquinone Based on Porous Co3O4 Nanorods Embellished Chemically Oxidized Carbon Black. *Food Control* **2022**, *136*, 108844.

(52) Prinith, N. S.; Manjunatha, J. G.; Albaqami, M. D.; Mohamed Tighezza, A.; Sillanpää, M. Electrochemical Analysis of Food Additive Vanillin Using Poly (Aspartic Acid) Modified Graphene and Graphite Composite Paste Sensor. *ChemistrySelect* **2022**, *7* (48), No. e202203572.